
Title	Atmospheric microplasma based binary Pt ₃ Co nanoflowers synthesis
Author(s)	Ying Wang, Bo Ouyang, Bowei Zhang, Yadian Boluo, Yizhong Huang, Raju V Ramanujan, Kostya (Ken) Ostrikov and Rajdeep S. Rawat
Source	<i>Journal of Physics D: Applied Physics</i> , 53(22), Article 225201
Published by	IOP Publishing

Copyright © 2020 IOP Publishing

This is an author-created, un-copyedited version of an article accepted for publication in *Journal of Physics D: Applied Physics*. The publisher is not responsible for any errors or omissions in this version of the manuscript or any version derived from it. The Version of Record is available online at <https://doi.org/10.1088/1361-6463/ab7797>

Citation: Wang, Y., Ouyang, B., Zhang, B., Boluo, Y., Huang, Raju V. Ramanujan, Ostrikov, K. & Rawat, R. S. (2020). Atmospheric microplasma based binary Pt₃Co nanoflowers synthesis. *Journal of Physics D: Applied Physics*, 53(22), Article 225201. <https://doi.org/10.1088/1361-6463/ab7797>

Atmospheric microplasma based binary Pt₃Co nanoflowers synthesis

Ying Wang,^{1,2,†,a)} Bo Ouyang,^{1,2,†} Bowei Zhang,^{3,4} Yadian Boluo,⁴ Yizhong Huang,⁴ R. V. Ramanujan,⁴ Kostya (Ken) Ostrikov^{5,6} and R. S. Rawat^{2,a)}

¹ School of Science, Nanjing University of Science and Technology, 200 Xiao Ling Wei Street, Nanjing, China 210094

² National Science and Science Education (NSSE), National Institute of Education (NIE), Nanyang Technological University, 1 Nanyang Walk, Singapore 637616

³ Institute for Advanced Materials and Technology, University of Science and Technology Beijing, Beijing, China 100083

⁴ School of Material Science and Engineering (MSE), Nanyang Technological University, 50 Nanyang 8 Avenue, Singapore 639798

⁵ School of Chemistry, Physics and Mechanical Engineering, Queensland University of Technology, Brisbane, QLD 4000, Australia

⁶ CSIRO-QUT Joint Sustainable Processes and Devices Laboratory, P.O. Box 218, Lindfield, NSW 2070, Australia

a) E-mail: rajdeep.rawat@nie.edu.sg; wying813@njust.edu.cn

† Y. Wang and B. Ouyang contributed equally to this work.

Abstract

The atmospheric microplasma in gas-liquid phase technique serves as a new potential efficient and green catalyst preparation technique to fabricate nanomaterials. Due to the presence of diverse reactive species, this technique can promote rapid complex reactions in solutions, which are typically sluggish in traditional chemical processes. Here, atmospheric microplasma induced liquid chemistry (AMILC) is applied to fabricate three-dimensional (3D) binary Pt₃Co nanoflowers. Nano-architectures of Pt₃Co bimetals (2D nanosheets and 3D nanoflowers) can be formed by tuning the initial cobalt molar concentration in the solution. 3D nanoflowers show a “nano-bouquet” like nanostructure with Co-oxide forming leaves and Pt₃Co forming waxberries. 3D nanoflowers show promising electrocatalytic behavior towards ethanol and glucose sensing in alkaline condition. Additionally, AMILC takes less synthesis duration (~10 min) without hazardous chemicals for Pt₃Co bimetal nanostructure preparation compared to conventional chemical approaches (>2 h), indicating that AMILC is a potential candidate with better energy efficiency, lower carbon footprint and green plasma chemistry process for 3D nanostructure material synthesis in catalyst applications.

Keywords: atmospheric microplasma, binary Pt-Co nanoflowers, 3D nanostructure, electrocatalyst

1. Introduction

Bimetallic nanoparticles are of great interest due to their wide applications in catalysis [1-3], sensors [4], optics [5], electronics [6], biomedicine [7], magnetics [8], etc. To date, bimetallic catalysts are typically prepared by electrodeposition [9], thermal deposition [10], self-assembly approach [11], and galvanic replacement reaction [12]. However, these techniques are inevitably time-consuming with the introduction of environmentally hazardous species (such as oleic acid, ammonia, etc.). Moreover, traditional thermal methods usually induce sintering and encounter challenges in handling heat-sensitive substrates [13; 14], such as soft materials, ultrahigh-surface-area carbon, nanosized porous polymer and covalent organic framework. Hence, novel techniques, including plasma [15; 16], microwave heating [17], ultrasonic treatment [18], pyrolysis of ionic liquids [19], electrospinning [20] and bioreductive approach [21], have been developed. Among these innovative strategies, non-thermal plasma has received considerable interest due to its promising potential in green catalyst preparation.

Non-thermal plasma contains reactive species involving electrons, ions, radicals, photons, and excited molecules. The electron temperature of the plasma can reach thousands of degrees ($10^5\sim 10^6$ K), but its ion (or gas) temperature remains low, typically around room temperature (298.15 K). Such reactive electronic states in non-thermal plasma enables rapid fabrication even in mild condition. Additionally, high reactivity at the plasma-substrate interfaces at low temperatures results in controllable reaction, leading to preservation of bulk material as well as distinct nano-structural morphologies. For instance, both FeCuSi-C [22] and NiPt/MgAlO [23] catalyst prepared by plasma-assisted processes exhibited higher dispersion and smaller particle size distribution. The high dispersion led to more active components exposed on the surface. As a result, these catalysts exhibited higher activity, improved selectivity and better stability than those synthesized by conventional methods [22; 23]. Bimetals like Ag/Au colloidal nanoparticles [24], Au-Pd nanoparticles [25] and PtPd core-shell structure with Pt as the shell [26] have also

been mostly prepared by glow discharge plasma. However, there are very few reports on alloy fabrication by atmospheric microplasma (AMP).

AMP refers to electrical discharges, carried out at atmospheric pressure, where at least one of the dimensions of the plasma is of sub-millimeter length scale [27]. Compared to other plasmas, AMP shows advantages of low cost, negligible thermal effects and high electron density due to the absence of a vacuum chamber and a micro-plasma tube. It has been reported that 0D, 1D and 2D nanostructured metal and metal oxide materials can be successfully synthesized via such strategies [28-30]. To date, there is only a few reports on the fabrication of 3D catalytic nanostructures by AMP. Well-controlled 3D Pt nanostructures (e.g. dendrites and nanoflowers) are reported to be particularly interesting due to their high electrochemically active surface area and high catalytic activity [31-34]. 3D nanostructuring also implies less metal, which could reduce cost, especially for Pt [31; 32]. Here, we report a novel AMILC method for controllably synthesizing 2D and 3D binary Pt₃Co nanoflowers. The catalytic properties of these bimetallic nanoflowers are also investigated.

2. Experimental Section

The AMP setup is shown in Figure 1. A DC AMP discharge with constant current of 2 mA (using TREK 615-10, ±10 kV AC/DC generator) was sustained between the hollow stainless steel anode (of Ø 700 µm bore diameter) and the surface of the aqueous electrolyte contained in a glass vessel. The tip of the anode was placed 2 mm above the surface of the electrolyte. The electrolyte was prepared by dissolving 0.002 M chloroplatinic acid hydrate (H₂PtCl₆·xH₂O), variable molar concentration of cobalt(II) sulfate heptahydrate (CoSO₄·7H₂O) and 0.5 M sodium sulfate (Na₂SO₄) in 40 mL of distilled water. Different concentrations of CoSO₄·7H₂O (0.4, 0.5, 0.6 and 0.8 M) were investigated. Helium gas at flow rate of 50 sccm was used as the discharge medium. The experiments were conducted for a fixed AMP discharge duration of 10 min. Bimetallic Pt-Co nanostructures were formed on the cathodic Si substrate half-inserted in the aqueous electrolyte at a distance of at least 3 cm from the anodic capillary, as shown in Figure 1.

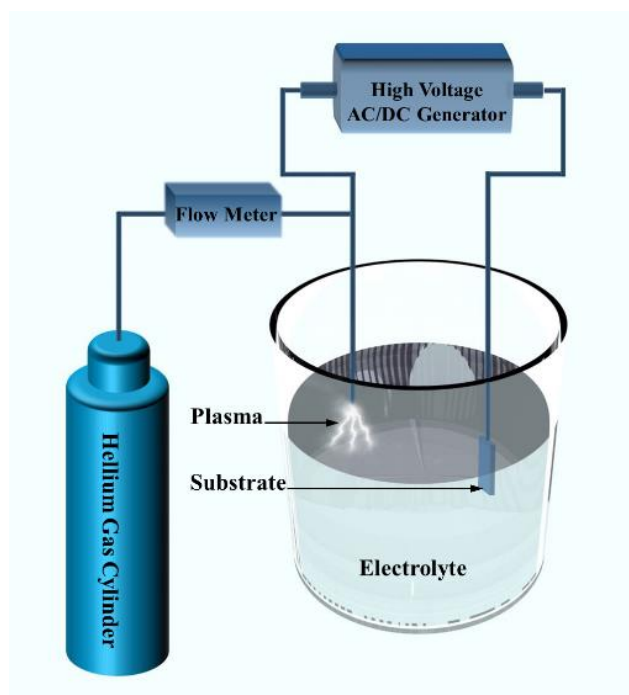


Figure 1 Schematic diagram of the atmospheric microplasma-induced liquid chemistry synthesis method.

All reagents were purchased from Sigma Aldrich Singapore and used as received without further purification. The Si substrate (1 cm × 2 cm) was cleaned sequentially in acetone, ethanol and deionized water for 10 min each in an ultrasonic bath before experiment. The morphology and size of the prepared nanostructures were determined by a JEOL JSM-6700F Field Emission Scanning Electron Microscope (FESEM) at 5 kV and a JEOL 2100F Transmission Electron Microscope (TEM). The composition of the nanoflowers was determined by a Oxford Instrument Energy Dispersive X-ray (EDX) spectroscopy system attached to the FESEM, an EDAX EDX Detector attached to the TEM, and by X-ray diffraction (Shimadzu XRD-6000). The crystallization of the nanoflowers was also investigated by XRD and TEM. The XRD was operated at 40 kV and 30 mA with Cu K_α radiation and a scan speed of 0.4 °/min. Electrochemical measurements were performed using an AUTOLAB PGSTAT 302N electrochemical workstation (Metrohm Pte Ltd, Switzerland). The deposited Pt₃Co sample (0.40 cm × 0.75 cm) was used as the working electrode. Ag/AgCl electrode and Pt foil (1.5 cm × 1.5 cm) were used as the reference electrode and the counter electrode, respectively.

3. Results and discussion

The nanoflowers with average diameter of ~ 756 nm and average height of ~ 416 nm in a solution with optimized 0.6 M CoSO_4 were confirmed by the low magnification SEM images in Figure 2(a) and (b). SEM image in Figure 2(c) indicates an average petal thickness of single nanoflower of ~ 8 nm. The TEM image in Figure 2(d) shows nanoflowers that look like a string of nano-waxberries, with Co-oxides forming the nano-leaves and Pt_3Co forming the nano-waxberries. All these compositions are confirmed by TEM EDX results in Figure 3 and XRD in Figure 4(a). The nano-waxberries have an average diameter of 128 ± 25 nm. The high magnification image of a single “nano-waxberry” (Figure 2(e)) shows that the nano-waxberry consists of nanoparticles with diameter less than 10 nm.

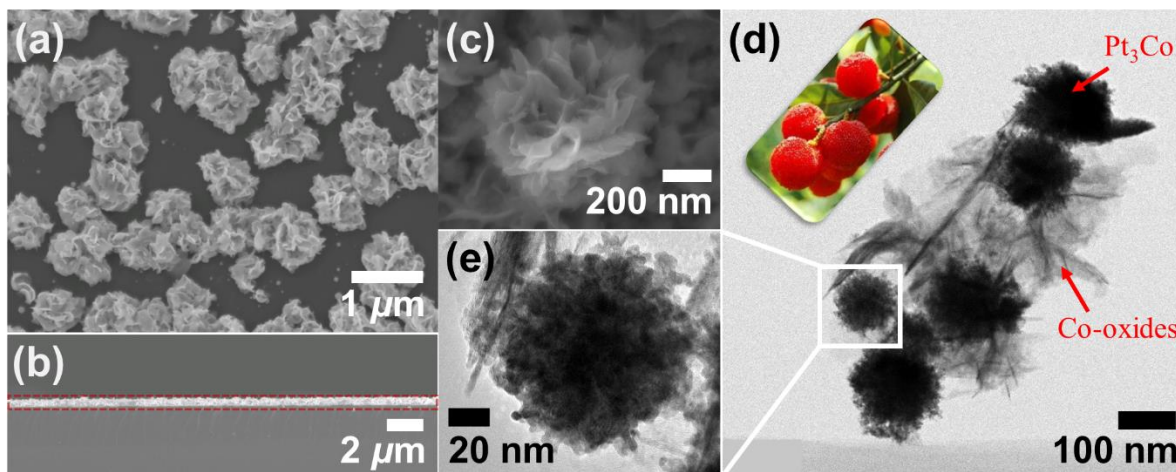


Figure 2 Morphology of nanoflowers: (a) low magnification SEM image of nanoflowers with average diameter of ~ 760 nm; (b) Cross-sectional SEM image of nanoflowers with an average height of ~ 416 nm; (c) high magnification SEM image of a single nanoflower; (d) low magnification TEM image of nanoflowers, which looks like a string of waxberry (inset); (e) high magnification TEM image of a single “nano-waxberry”.

The composition of nanoflowers was investigated by both EDX results of FESEM and TEM as shown in Figure 3(a-c) and confirmed by XRD and TEM FFT (Figure 4). Figure 3(a₁-a₃) are the EDX results of nanoflowers in FESEM image (Figure 3(a)). The nanoflowers mainly consist of Pt and Co with an average atomic percentage of 27.8 and 12.1, respectively, which means that the atomic ratio of Pt:Co is 2.3:1 (Figure S1). Figure 3(b₁-b₃) show the EDX results of the “string of waxberries” in TEM images (Figure 2(d) and Figure 3(b)). The nano-waxberries are mainly composed of Pt and Co, while the nano-leaves are formed by both Co and O. The total atomic percentage of Pt, Co and O is 8.8, 11.5 and 19.0, respectively (Figure S2). Assuming the atomic ratio of Pt:Co obeys 2.3:1 as shown in Figure 3(a₁) and (a₂), the atomic ratio of the rest Co to O (Co:O) is 1:2.5. The EDX result (Figure 3(c₁-c₃)) of the quarter part of a nano-waxberry further

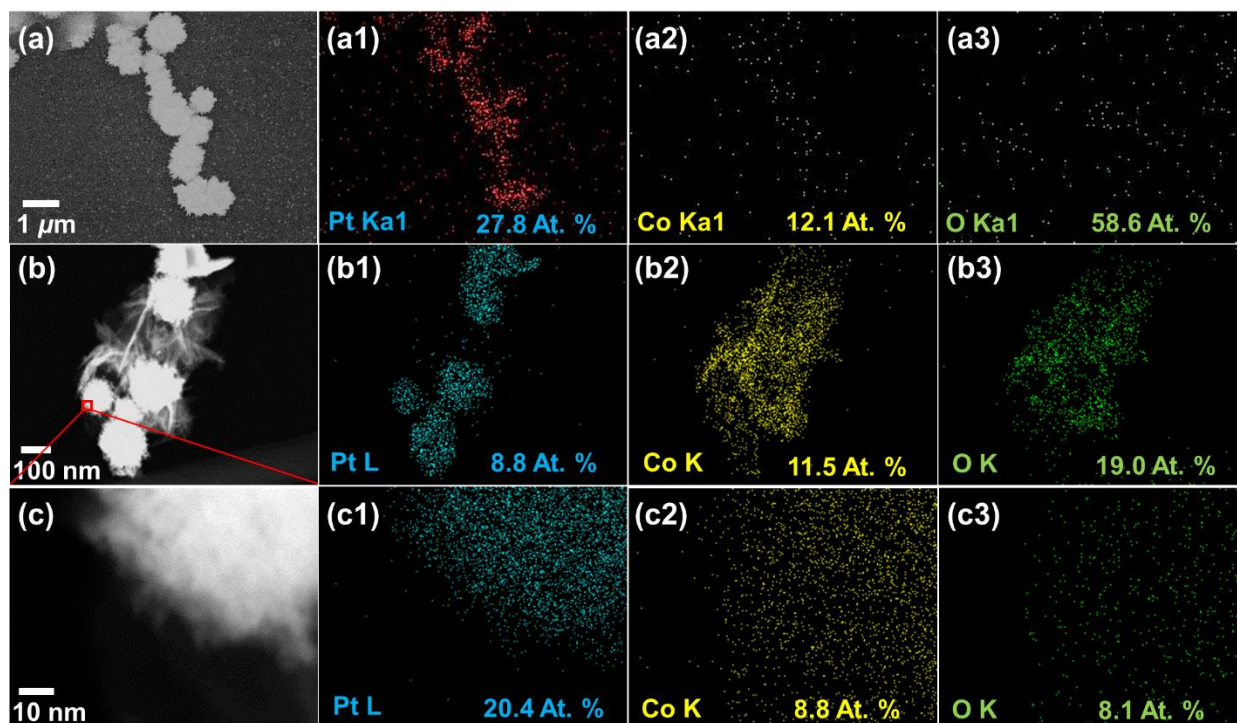


Figure 3 Composition of nanoflowers evidenced by (a) FESEM EDX results and (b-c) TEM EDX results: (a) morphology of nanoflowers for elemental mapping in FESEM, (a₁-a₃) elemental mapping of (a₁) Pt, (a₂) Co and (a₃) O; (b) low magnification morphology of nanoflowers for elemental mapping in TEM, (b₁-b₃) elemental mapping of (b₁) Pt, (b₂) Co and (b₃) O; (c) high magnification morphology of the quarter part of a “nano-waxberry” for elemental mapping in TEM, (c₁-c₃) elemental mapping of (c₁) Pt, (c₂) Co and (c₃) O.

reveals that the nano-waxberry mainly consists of Pt and Co, with atomic percentage of 20.4 and 8.8, respectively (Figure S3). The atomic ratio of Pt:Co is 2.3:1, which coincides with that of the EDX results from FESEM in Figure 3(a₁-a₃). Hence, both the EDX results from FESEM and TEM suggest that the nanoflowers are composed of cobalt-platinum alloy with a composition of Pt_{2.3}Co. However, there could be impurities of cobalt oxides in the nanoflowers, as shown in the XRD diffraction pattern (Figure 4(a)).

Figure 4 shows the XRD pattern, TEM images and the related FFT pattern of the as-deposited nanoflower sample. The XRD pattern of the nanoflower sample (Figure 4(a)) matches well with the standard diffraction pattern of cubic Pt₃Co (PDF #00-029-0499), confirming the composition of Pt₃Co for nanoflowers. The diffraction peaks at 2θ values of $\sim 121^\circ$ and $\sim 127^\circ$ matches well with (331) and (420) facets respectively, indicating the face centered cubic (FCC) Pt₃Co (PDF #00-029-0499). There are also two impurity peaks at 2θ values of $\sim 27^\circ$ and $\sim 34^\circ$, which might be assigned to the diffraction peak of Co₂O₃ at 28° (PDF #00-002-0770) and the diffraction peak of CoO at 34° (PDF #00-042-1300), respectively. However, only one peak matches with each standard data. Considering both the XRD and EDX results, it can be confirmed that the impurities are cobalt oxides. The composition of Pt₃Co for the nanoflower samples is further confirmed by FFT pattern in Figure 4(c). The FFT pattern shows the polycrystalline nature of the Pt₃Co nanoparticles, which coincides with the XRD result shown in Figure 4(a). The FFT pattern matches with FCT Pt₃Co ICSD-107048 data using JEMS@JEOL, the structure of which is assigned to the PDF number #00-029-0499 (experimental powder diffraction data). Coincidentally, this standard PDF number is the same as the matched PDF number of the XRD diffraction pattern in Figure 4(a). It shows the formation of family of crystal planes corresponding to (111), (200), (220), (311), (222) and (331), all of which are also detected in the XRD pattern in Figure 4(a).

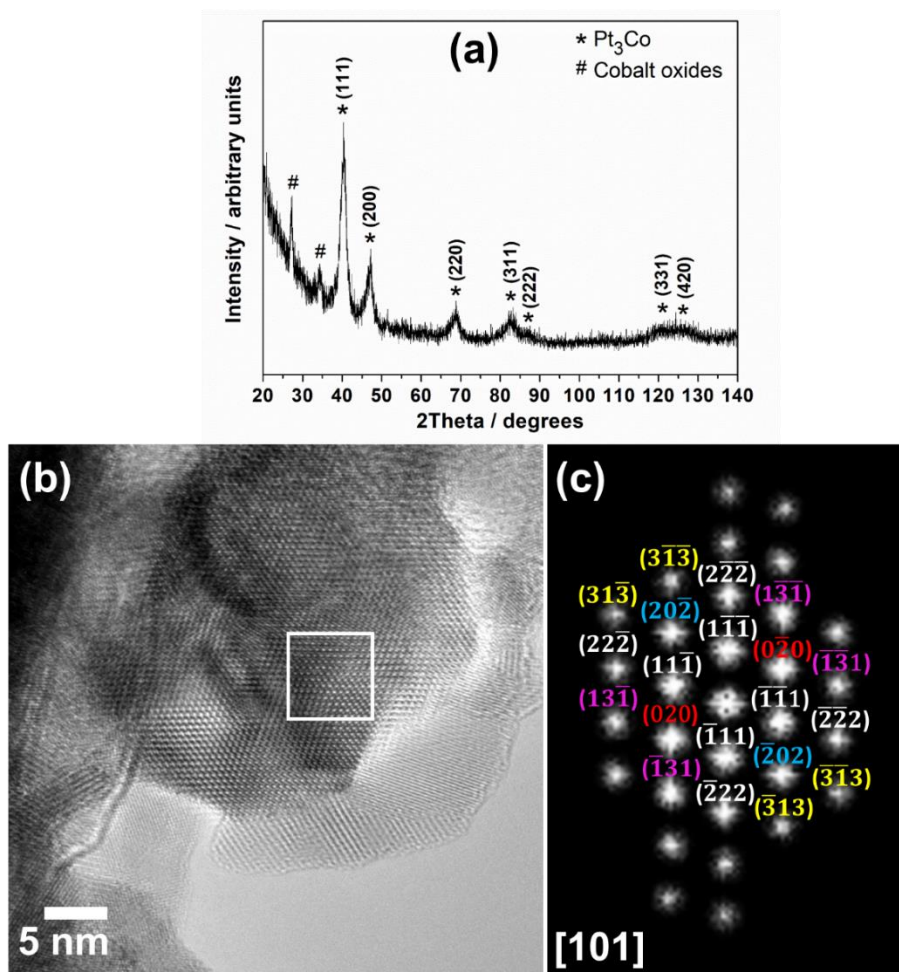


Figure 4 Crystallization of nanoflowers by (a) XRD and (b) TEM: (a) XRD patterns of the nanoflower sample matching with standard data of Pt_3Co ; (b) High resolution TEM images of Pt_3Co nanoparticles from the nanoflower sample; (c) Fast Fourier Transform (FFT) pattern for Pt_3Co nanoparticle shown in (b).

The reason for the growth of 3D Pt_3Co nanoflowers at 0.6 M CoSO_4 can be understood from Figure 5 and Figure 6. The lower CoSO_4 concentration of 0.4 and 0.5 M results in porous ultrathin and thicker nanosheets, respectively. The increase in Co-precursor concentration from 0.4 to 0.5 M leads to greater thickness of 2D nanosheets but the concentration is insufficient to result in 3D nanostructures. At 0.6 M CoSO_4 concentration there is substantial amount of Co that allows the growth of 3D nanoparticle agglomerate (called nanoseeds), shown in Figure 6(a), as opposed to nanosheets. The formation of nanoseeds is the precondition for 3D nanoflower

formation. This is evident from the growth sequences of nanoflowers shown in Figure 6(a-d), which shows different stages of nanoflower formation observed by carefully scanning different parts of the 3D nanoflower sample. Some nanoparticle nucleation on the 0.6 M CoSO_4 sample might have started at later time instants. Hence, we can observe different stages of nanoflower formation on the same sample surface, which helps us determine the nanoflower formation mechanism. Once the higher concentration of Co elements (in 0.6 M CoSO_4) allows formation of 3D nanoseeds (Figure 6(a), showing spherical agglomeration of numerous nanoparticles), nanopetals start to grow from their surface (Figure 6(b)). This is followed by anisotropic growth of nanopetals (Figure 6(c)) to full growth of nanoflowers (Figure 6(d)) within 10 min AMP discharge duration. Further increase in CoSO_4 concentration to 0.8 M results in thicker rice-like nanorods (Figure 5(d)) rather than nanoflowers.

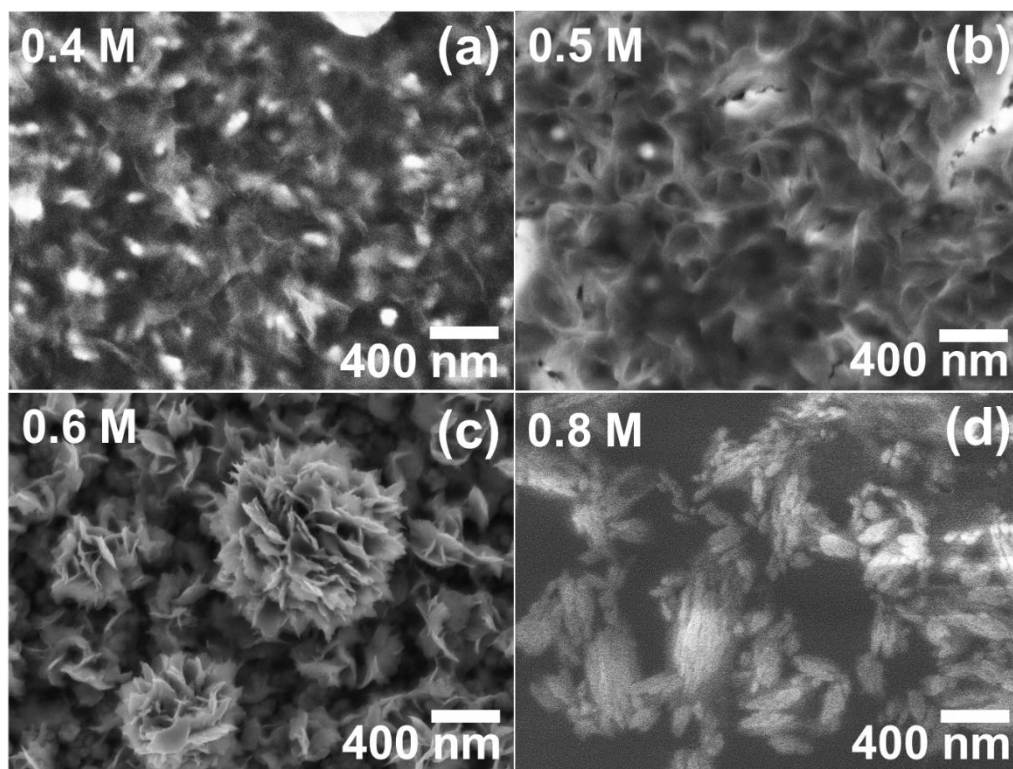


Figure 5 Variety of fabricated nanostructures using atmospheric microplasma (AMP) induced liquid chemistry method with increasing initial molar concentration of CoSO_4 solvent: (a) thin nanosheets with 0.4 M CoSO_4 , (b) thick anisotropic nanosheets with 0.5 M CoSO_4 , (c) nanoflowers with 0.6 M CoSO_4 and (d) rice-like nanorods with 0.8 M CoSO_4 .

The growth stages of the nanoflowers are further confirmed via increasing plasma discharge duration from 2 to 10 min (0.6 M CoSO₄) in Figure 6(e-g). At 2 min plasma discharge (Figure 6(e)), small nanoseeds (average diameter 74 ± 35 nm in Figure S4) are formed by agglomeration of nanoparticles (<10 nm). With an increase of plasma discharge duration to 5 min (Figure 6(f)), more nanoparticles agglomerate to form larger nanoseeds (average diameter 130 ± 65 nm in Figure S4), providing the foundation for nanopetal growth. Some isolated nanopetals start to grow on nanoseeds by the end of 5 min AMP discharge. With an increase of plasma discharge duration to 10 min (Figure 6(g)), nanopetals grow anisotropically and finally form nanoflowers. The average size at this stage is 284 ± 145 nm (Figure S4). Longer plasma discharge duration leads to enhanced 3D agglomeration of nanoparticles, followed by the growth of nanopetals and nanoflowers. Hence, it can be concluded that the formation of nanoflowers starts from the formation of 3D nanoseeds due to 3D agglomeration of nanoparticles, which happens at the optimum Co-precursor concentration of 0.6 M; followed by growth of nanopetals on those nanoseeds and completed by the growth of nanoflowers due to anisotropic growth of nanopetals

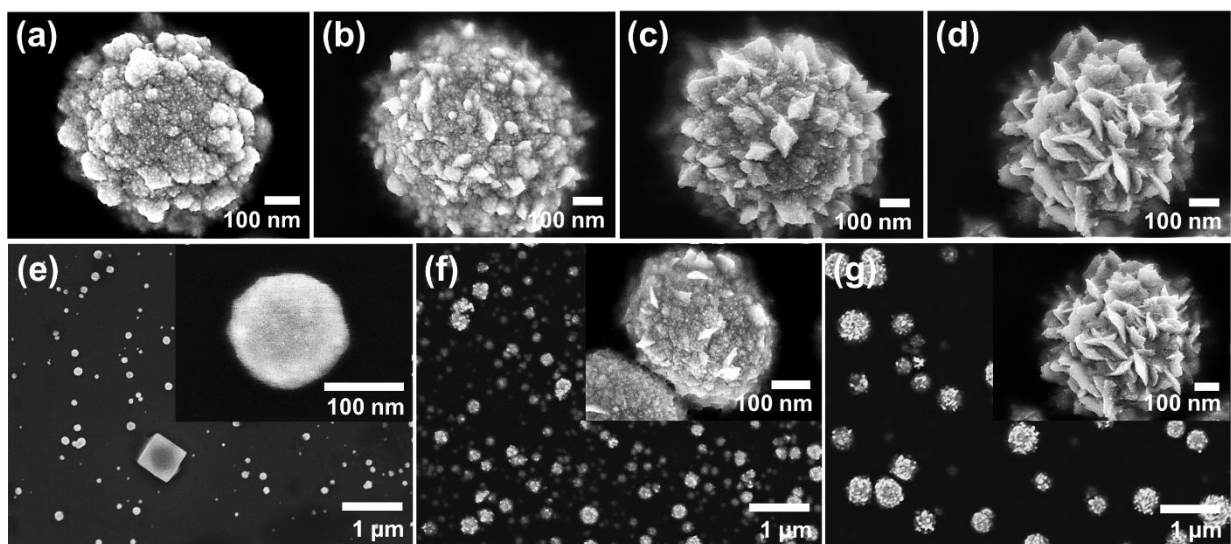


Figure 6 The growth stages of 3D nanoflowers (a-d) at different part on the nanoflower sample with 0.6 M CoSO₄ concentration, (a) nanoseeds formed by three-dimensional agglomeration of nanoparticles, (b) nanopetals growing on nanoseeds, (c) anisotropic growth of nanopetals, and (d) full growth of nanoflowers; as well as (e-g) with the increasing plasma discharge duration from (e) 2 min, (f) 5 min to (g) 10 min, insets show their respective high magnification images.

(with optimum plasma discharge duration of ~10 min).

The comparison of in-plane and out-of-plane magnetic properties for both nanosheet and nanoflower samples (0.4 M CoSO₄ and 0.6 M CoSO₄ samples, respectively) is shown in Figure 7. The coercivities of all samples are less than 800 G even after thermal annealing (600°C 1 h), indicating that both nanosheet and nanoflower samples are relatively soft for usage in data storage applications, which is one of the common applications for Pt-Co bimetallic nanomaterials.

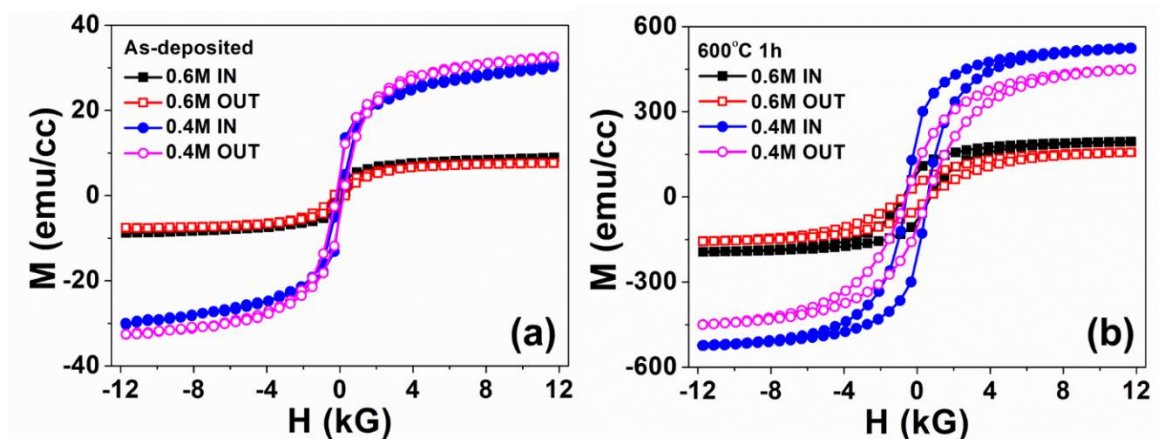


Figure 7 Both in-plane and out-of-plane magnetic properties of nanosheets (0.4 M CoSO₄) and nanoflowers (0.6 M CoSO₄): (a) as-deposited samples, and (b) after 600°C thermal annealing for 1 h.

The larger surface area of 3D nanoflowers than 2D nanosheets, proved by the smaller water contact angle of nanoflowers (43°) than that of nanosheets (69°) (Figure S5), suggests potential applications in electrochemical catalysis. We have earlier reported in our previous work [35] that the larger surface area leads to better electrochemical activities for nanoflower samples than nanosheet samples in N₂-saturated 0.5 M H₂SO₄ with 1 M methanol. An approximate electrochemically active surface area (ECSA) of 5.76 cm²·g_{Pt}⁻¹ is estimated from the cyclic voltammograms (CV) curve of nanoflower (Figure S6, along with detailed explanation) according to literature [36]. The current density of nanoflower sample (Figure S6) is much higher than that of nanosheets, indicating the better activity of 3D nanoflower than 2D nanosheet in acidic environment. Further characterization of electrochemical activities of 3D nanoflowers

in alkaline (NaOH) solution towards ethanol and glucose sensing has been performed. The cyclic voltammograms (CV) curves of Pt₃Co nanoflowers (Figure S7) suggests great electrochemical reactivity for the sample in 0.2 M NaOH solution. The CV curves with scan range of both 0.05-1.00 V and 0.05-0.80 V presents constant redox peaks, indicating no difference between the two scan ranges. Hence, the rest of the CV curves were performed in 0.2 M NaOH with maximum scan potential of 0.80 V.

The CV curves of Pt₃Co nanoflowers in NaOH solution with either ethanol (Figure 8(a)) or glucose (Figure 8(b)) indicate that Pt₃Co nanoflowers can be useful for electrochemical sensing of both ethanol and glucose. Figure 8(a) presents the CV curves in the absence and presence of 1.0 M ethanol at a potential sweep rate of 10 mV·s⁻¹. In the absence of ethanol, the large anodic current density indicates Pt₃Co nanoflowers is useful for electrochemical sensing applications [37]. The oxidation and reduction peaks located at ~0.64 V and ~0.18 V are observed, which might be assigned to Co³⁺ oxidation and Co³⁺ reduction [37; 38], respectively. The constant peak potentials with 20 scan cycles indicate promising stability of the nanoflower sample. In the presence of ethanol, the narrow hysteresis between the positive and negative sweeps indicates decreased adsorbed intermediates on the catalytic surface as the surface might be blocked by ethanol decomposition [39]. Figure 8(b) shows the CV curves of Pt₃Co nanoflowers in 0.2 M NaOH solution with and without 4 mM glucose at a scan rate of 10 mV·s⁻¹. In the absence of glucose, the reduction peak located at ~0.2 V at the first cycle might be assigned to Co³⁺ reduction [37; 38]. It shifts negatively and becomes constant with increased scan cycles. Upon addition of 4 mM glucose, a large enhancement of the anodic peak current density indicates the efficiency of Pt₃Co nanoflowers for electro-oxidation of glucose [38].

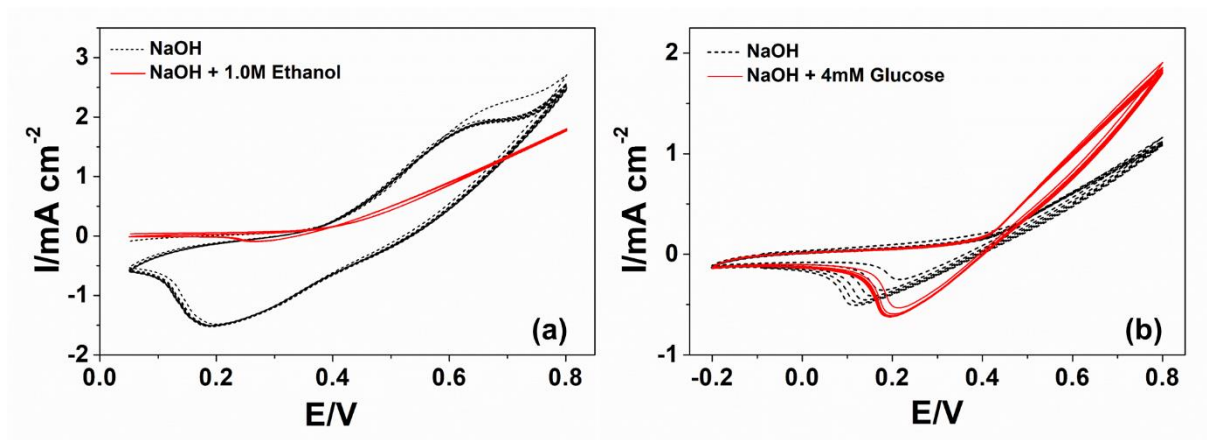


Figure 8 Cyclic Voltammograms of Pt₃Co nanoflowers in 0.2 M NaOH (a) in the absence of ethanol (black dash line) and in the presence of 1.0 M ethanol (red solid lines); and (b) in the absence of glucose (black dash line) and in the presence of 4 mM glucose (red solid line); Scan rate: 10 mV·s⁻¹.

4. Conclusions

In summary, 3D nanoflowers have been successfully prepared by AMILC with short fabrication duration of 10 min. The nanoflowers look like “a string of nano-waxberries” with Co-oxides forming the nano-leaves and Pt₃Co forming the nano-waxberries. The nano-architectures can be tuned from 2D nanosheets to 3D nanoflowers and again to 2D nanorods by controlling the molar concentration of Co-based precursor. The nanoflowers were formed only at the concentration of 0.6 M CoSO₄·7H₂O. The magnetic properties of both the 2D and 3D samples are soft with coercivities less than 800 G from the data storage application point of view. Moreover, the catalytic properties of 3D nanoflowers are quite active for electrochemical sensing of methanol in acidic solution and of ethanol and glucose in alkaline solution. Compared to traditional fabrication approaches, AMILC method shows advantages of much shorter fabrication duration, tunability of nano-architecture, simple process and comparable catalytic properties of prepared samples. This suggests AMP-induced liquid chemistry can be competitive as a potential innovative method with advantages of better energy efficiency and eco-friendly strategy for 3D nanostructure synthesis in catalyst applications. Practical applications for a broad range of catalyst material need to be tested and established.

Acknowledgments

This project was funded by “China Postdoctoral Science Foundation No. 2018M640486” and “Fundamental Research Funds for the Central Universities No. 30919011248”. The authors are also grateful to the National Institute of Education, Nanyang Technological University Singapore, for providing the AcRF Grant RI 7/11 RSR.

References

- [1] Lee H, Lim J, Lee C, Back S, An K, Shin J W, Ryoo R, Jung Y and Park J Y 2018 Boosting hot electron flux and catalytic activity at metal-oxide interfaces of PtCo bimetallic nanoparticles *Nat. Commun.* **9** 2235
- [2] Pieta I S, Rathi A, Pieta P, Nowakowski R, Hołdyski M, Pisarek M, Kaminska A, Gawande M B and Zboril R 2019 Electrocatalytic methanol oxidation over Cu, Ni and bimetallic Cu-Ni nanoparticles supported on graphitic carbon nitride *Appl. Catal. B* **244** 272-83
- [3] Tian X, Zhao X, Su Y Q, Wang L, Wang H, Dang D, Chi B, Liu H, Hensen E J M, Lou X W and Xia B Y 2019 Engineering bunched Pt-Ni alloy nanocages for efficient oxygen reduction in practical fuel cells *Science* **366** 850-6
- [4] Amiripour F, Azizi S N and Ghasemi S 2018 Gold-copper bimetallic nanoparticles supported on nano P zeolite modified carbon paste electrode as an efficient electrocatalyst and sensitive sensor for determination of hydrazine *Biosens. Bioelectron.* **107** 111-7
- [5] Kadkhodazadeh S, Nugroho F A A, Langhammer C, Beleggia M and Wagner J B 2019 Optical property-composition correlation in noble metal alloy nanoparticles studied with EELS *ACS Photonics* **6** 779-86
- [6] Tan H W, An J, Chua C K and Tran T 2019 Metallic nanoparticle inks for 3D printing of electronics *Adv. Electron. Mater.* **5** 1800831
- [7] Breisch M, Grasmik V, Loza K, Pappert K, Rostek A, Ziegler N, Ludwig A, Heggen M, Epple M, Tiller J C, Schildhauer T A, Köller M and Sengstock C 2019 Bimetallic silver-platinum nanoparticles with combined osteo-promotive and antimicrobial activity *Nanotechnology* **30** 305101
- [8] Garnero C, Lepesant M, Garcia-Marcelot C, Shin Y, Meny C, Farger P, Warot-Fonrose B, Arenal R, Viau G, Soulantica K, Fau P, Poveda P, Lacroix L-M and Chaudret B 2019 Chemical ordering in bimetallic FeCo nanoparticles: from a direct chemical synthesis to application as efficient high-frequency magnetic material *Nano Lett.* **19** 1379-86
- [9] Oskueyan G and Mansour Lakouraj M 2019 Electrodeposition of nanostructured Pt-Pd bimetallic catalyst on polyaniline-camphorsulfonic acid/graphene nanocomposites for methanol electrooxidation *J. Appl. Electrochem.* **49** 755-65
- [10] Shi D, Yang Q, Peterson C, Lamic-Humblot A-F, Girardon J-S, Griboval-Constant A, Stievano L, Sougrati M T, Briois V, Bagot P A J, Wojcieszak R, Paul S and Marceau E 2019 Bimetallic Fe-Ni/SiO₂ catalysts for furfural hydrogenation: identification of the interplay between Fe and Ni during deposition-precipitation and thermal treatments *Catal.Today* **334** 162-72
- [11] Song S, Liu Y, Liu Q, Wu L, Long Y, Li J and Zhang H 2019 Tunable bimetallic Au-Pd@CeO₂ for semihydrogenation of phenylacetylene by ammonia borane *Nanoscale* **11** 12932-7
- [12] Anderson S R, Mohammadtaheri M, Kumar D, O'Mullane A P, Field M R, Ramanathan R and Bansal V 2016 Robust nanostructured silver and copper fabrics with localized surface plasmon

- resonance property for effective visible light induced reductive catalysis *Adv. Mater. Interf.* **3** 1500632
- [13] Wang Z, Zhang Y, Neyts E C, Cao X, Zhang X, Jang B W L and Liu C 2018 Catalyst preparation with plasmas: how does it work? *ACS Catal.* **8** 2093-110
- [14] Liu C, Li M, Wang J, Zhou X, Guo Q, Yan J and Li Y 2016 Plasma methods for preparing green catalysts: current status and perspective *Chinese J. Catal.* **37** 340-8
- [15] Ouyang B, Zhang Y, Xia X, Rawat R S and Fan H J 2018 A brief review on plasma for synthesis and processing of electrode materials *Mater. Today Nano* **3** 28-47
- [16] Hartl H, MacLeod J, O'Mullane A P, Motta N and Ostrikov K 2019 Multiscale plasma-catalytic on-surface assembly *Small* 1903184
- [17] Chen P, Xing P, Chen Z, Hu X, Lin H, Zhao L and He Y 2019 In-situ synthesis of AgNbO₃/g-C₃N₄ photocatalyst via microwave heating method for efficiently photocatalytic H₂ generation *J. Colloid Interface Sci.* **534** 163-71
- [18] Ma Z, Wu D, Han X, Wang H, Zhang L, Gao Z, Xu F and Jiang K 2019 Ultrasonic assisted synthesis of Zn-Ni bi-metal MOFs for interconnected Ni-N-C materials with enhanced electrochemical reduction of CO₂ *J. CO₂ Util.* **32** 251-8
- [19] Adamski J, Qadir M I, Serna J P, Bernardi F, Baptista D L, Salles B R, Novak M A, Machado G and Dupont J 2018 Core-shell Fe-Pt nanoparticles in ionic liquids: magnetic and catalytic properties *J. Phys. Chem. C* **122** 4641-50
- [20] Zhang Y, Deng D, Zhu X, Liu S, Zhu Y, Han L and Luo L 2018 Electrospun bimetallic Au-Ag/Co₃O₄ nanofibers for sensitive detection of hydrogen peroxide released from human cancer cells *Anal. Chim. Acta* **1042** 20-8
- [21] Kang N, Zhu N, Guo W, Shi C, Wu P and Wei X 2018 Efficient debromination of tetrabromobisphenol A (TBBPA) by Au/Fe@biocarbon derived from bioreduction precious metals *Chem. Eng. J.* **334** 99-107
- [22] Zhang H, Chu W, Xu H and Zhou J 2010 Plasma-assisted preparation of Fe-Cu bimetal catalyst for higher alcohols synthesis from carbon monoxide hydrogenation *Fuel* **89** 3127-31
- [23] Yu X P, Zhang F B, Wang N, Hao S X and Chu W 2014 Plasma-treated bimetallic Ni-Pt catalysts derived from hydrotalcites for the carbon dioxide reforming of methane *Catal. Lett.* **144** 293-300
- [24] Alwan A M, Khamis R A and Abdallah S M 2019 Well-controlled generation process of bimetallic Ag/Au colloidal nanoparticles by non-thermal plasma DC glow discharge *Iraqi J. Med. Sci.* **60** 1274-85
- [25] Chen Y, Wang H, Liu C-J, Zeng Z, Zhang H, Zhou C, Jia X and Yang Y 2012 Formation of monometallic Au and Pd and bimetallic Au-Pd nanoparticles confined in mesopores via Ar glow-discharge plasma reduction and their catalytic applications in aerobic oxidation of benzyl alcohol *J. Catal.* **289** 105-17
- [26] Wang W, Wang Z, Wang J, Zhong C J and Liu C J 2017 Highly active and stable Pt-Pd alloy catalysts synthesized by room-temperature electron reduction for oxygen reduction reaction *Adv. Sci.* **4** 1600486
- [27] Davide M and Sankaran R M 2010 Microplasmas for nanomaterials synthesis *J. Phys. D: Appl. Phys.* **43** 323001
- [28] Haq A U, Askari S, McLister A, Rawlinson S, Davis J, Chakrabarti S, Svrcak V, Maguire P, Papakonstantinou P and Mariotti D 2019 Size-dependent stability of ultra-small α -/ β -phase tin nanocrystals synthesized by microplasma *Nat. Commun.* **10** 817
- [29] Borude R R, Sugiura H, Ishikawa K, Tsutsumi T, Kondo H, Ikarashi N and Hori M 2019 Single-step, low-temperature simultaneous formations and in situ binding of tin oxide nanoparticles to graphene nanosheets by in-liquid plasma for potential applications in gas sensing and lithium-ion batteries *ACS Appl. Nano Mater.* **2** 649-54

- [30] Chiang W-H, Mariotti D, Sankaran R M, Eden J G and Ostrikov K 2019 Microplasmas for Advanced Materials and Devices *Adv. Mater.* 1905508
- [31] Chen X M, Su B Y, Wu G H, Yang C J, Zhuang Z X, Wang X R and Chen X 2012 Platinum nanoflowers supported on graphene oxide nanosheets: their green synthesis, growth mechanism, and advanced electrocatalytic properties for methanol oxidation *J. Mater. Chem.* **22** 11284-9
- [32] Tiwari J N, Tiwari R N and Lin K L 2010 Synthesis of Pt nanopetals on highly ordered silicon nanocones for enhanced methanol electrooxidation activity *ACS Appl. Mater. Interfaces* **2** 2231-7
- [33] Yao Z Q, Zhu M S, Jiang F X, Du Y K, Wang C Y and Yang P 2012 Highly efficient electrocatalytic performance based on Pt nanoflowers modified reduced graphene oxide/carbon cloth electrode *J. Mater. Chem.* **22** 13707-13
- [34] Wei L, Fan Y J, Wang H H, Tian N, Zhou Z Y and Sun S G 2012 Electrochemically shape-controlled synthesis in deep eutectic solvents of Pt nanoflowers with enhanced activity for ethanol oxidation *Electrochim. Acta* **76** 468-74
- [35] R. S. Rawat and Wang Y 2017 *Advances in magnetic materials: processing, properties, and performance*, ed Sam Zhang and D Zhao (Singapore: CRC Press) pp 189-292
- [36] Wang W, Wang Z, Yang M, Zhong C-J and Liu C-J 2016 Highly active and stable Pt (111) catalysts synthesized by peptide assisted room temperature electron reduction for oxygen reduction reaction *Nano Energy* **25** 26-33
- [37] Premlatha S, Sivasakthi P and Ramesh Babu G N K 2015 Electrodeposition of a 3D hierarchical porous flower-like cobalt-MWCNT nanocomposite electrode for non-enzymatic glucose sensing *RSC Adv.* **5** 74374-80
- [38] Liu Y, Cao X, Kong R, Du G, Asiri A M, Lu Q and Sun X 2017 Cobalt phosphide nanowire array as an effective electrocatalyst for non-enzymatic glucose sensing *J. Mater. Chem. B* **5** 1901-4
- [39] Ma L, Chu D and Chen R 2012 Comparison of ethanol electro-oxidation on Pt/C and Pd/C catalysts in alkaline media *Int. J. Hydrogen Energy* **37** 11185-94

Electronic Supplementary Information

Atmospheric microplasma utilized for binary Pt₃Co nanoflowers synthesis

Ying Wang,^{1,2,†,a)} Bo Ouyang,^{1,2,†} Bowei Zhang,^{3,4} Yadian Boluo,⁴ Yizhong Huang,⁴ R. V. Ramanujan,⁴ Kostya (Ken) Ostrikov^{4,5} and R. S. Rawat^{2,a)}

¹ School of Science, Nanjing University of Science and Technology, 200 Xiao Ling Wei Street, Nanjing, China 210094

² National Science and Science Education (NSSE), National Institute of Education (NIE), Nanyang Technological University, 1 Nanyang Walk, Singapore 637616

³ Institute for Advanced Materials and Technology, University of Science and Technology Beijing, Beijing, China 100083

⁴ School of Material Science and Engineering (MSE), Nanyang Technological University, 50 Nanyang 8 Avenue, Singapore 639798

⁵ School of Chemistry, Physics and Mechanical Engineering, Queensland University of Technology, Brisbane, QLD 4000, Australia

⁶ CSIRO-QUT Joint Sustainable Processes and Devices Laboratory, P.O. Box 218, Lindfield, NSW 2070, Australia

a) E-mail: rajdeep.rawat@nie.edu.sg; wying813@njust.edu.cn

† Y. Wang and B. Ouyang contributed equally to this work.

Content

S1. FESEM EDX result for nanoflowers

S2. TEM EDX result for “string of waxberries”

S3. TEM EDX result for the quarter part of a nano-waxberry

S4. Variation of nanostructure size with increasing plasma discharge duration

S5. Comparison of surface area between nanoflowers and nanosheets

S6. Cyclic voltammograms (CV) of nanoflowers and nanosheets in acidic solution

S7. CV of Pt₃Co nanoflowers in NaOH solution with different molar concentration and different sweep range

S1. FESEM EDX result for nanoflowers

The FESEM EDX result is shown in Figure S1. Five sets of FESEM EDX data, shown in the inset table in Figure S1, were applied to calculate the average atomic percentage of cobalt, platinum and oxygen elements in the nanoflowers, respectively. The average atomic percentage of Co, Pt and O is 12.1, 27.8 and 60.1, respectively. Hence, the calculated atomic ratio of Pt:Co is approximately 2.3:1.

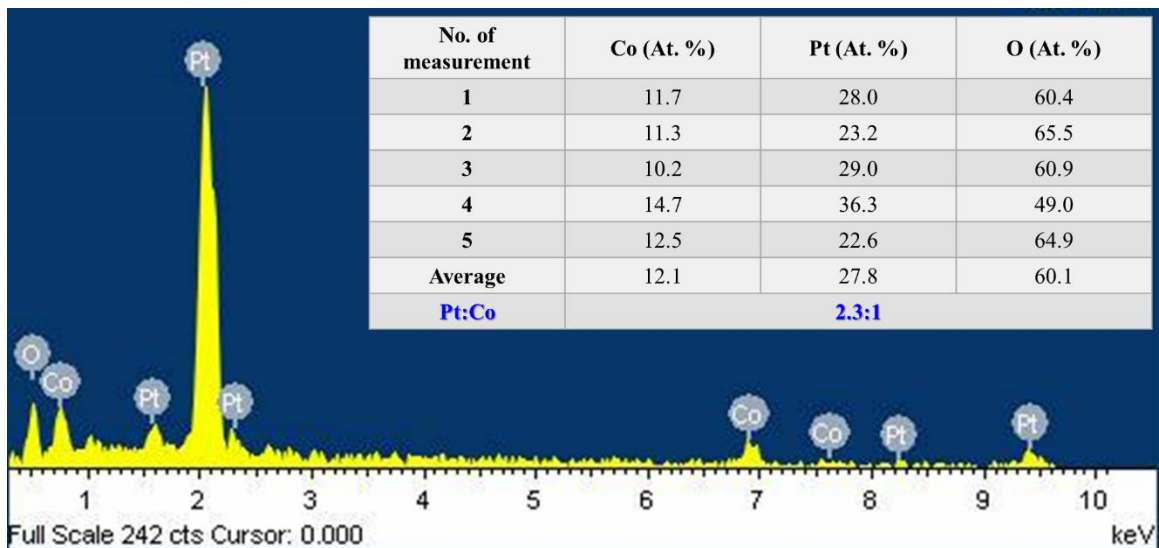


Figure S1 The FESEM EDX result for nanoflowers; the inset table shows 5 sets of atomic percentage of Co, Pt and O in FESEM EDX data, their average values and the calculated atomic ratio of Pt:Co.

S2. TEM EDX result for “string of waxberries”

The TEM EDX result of “string of waxberries” is shown in Figure S2. The atomic percentage of Co, Pt and O is 11.5, 8.8 and 19.0, respectively. The appearance of Cu and C in the results are due to the copper coated carbon grid used for TEM sample preparation.

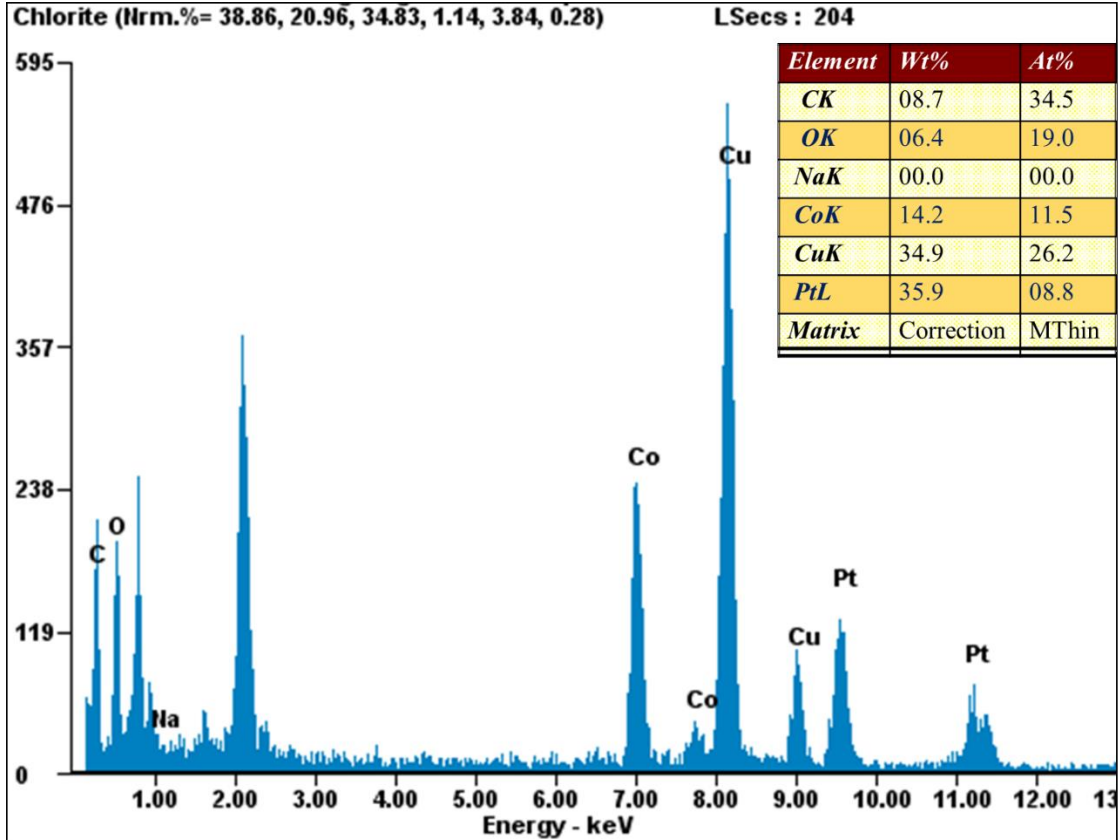


Figure S2 The TEM EDX result for “string of waxberries”; the inset table shows the atomic percentage of Co, Pt and O elements.

S3. TEM EDX result for the quarter part of a nano-waxberry

The TEM EDX result of the quarter part of a nano-waxberry is shown in Figure S3. The atomic percentage of Co, Pt and O is 8.8, 20.4 and 8.1, respectively. The atomic ratio of Pt:Co is around 2.3:1.

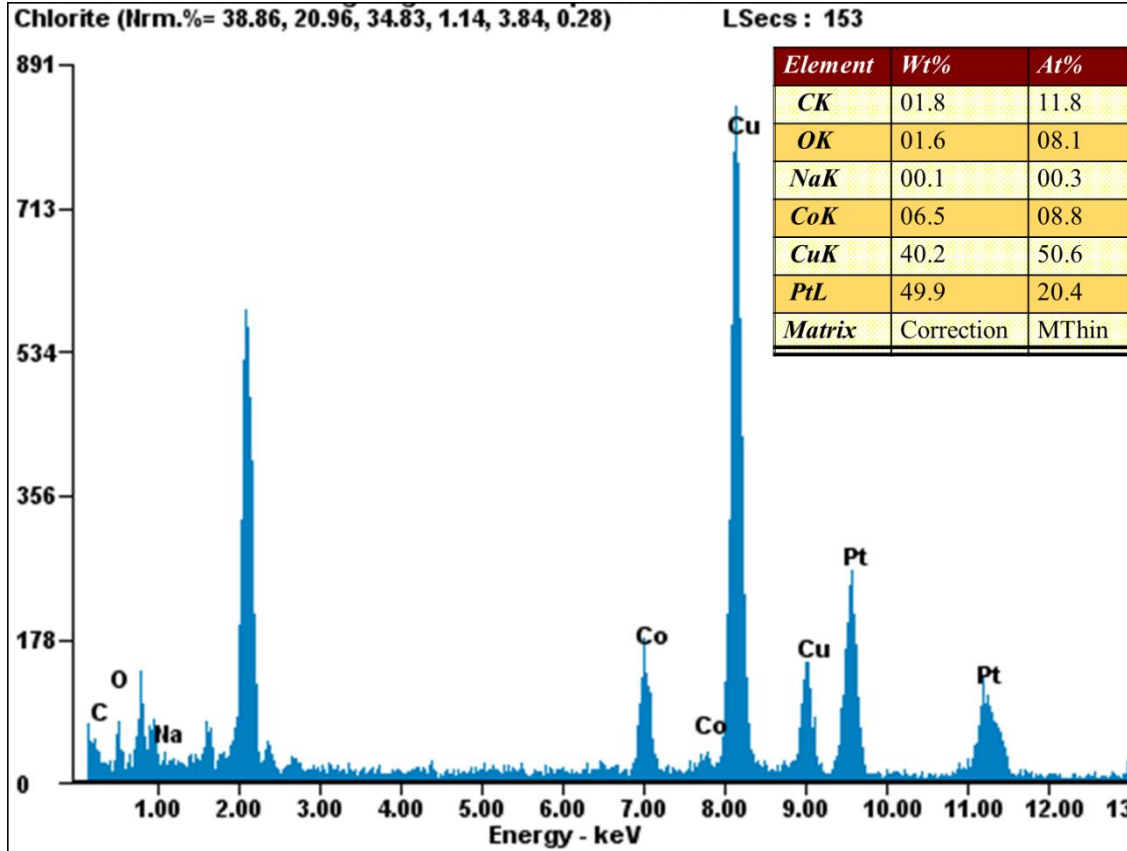


Figure S3 The TEM EDX result for the quarter part of a nano-waxberry; the inset table shows the atomic percentage of Co, Pt and O elements.

S4. Variation of nanostructure size with increasing plasma discharge duration

The variation of nanostructure size with increasing plasma discharge duration from 2 min, 5 min to 10 min is shown in Figure S4. The nanostructure size increases with increasing plasma discharge duration. The average diameter of nanoseeds formed at 2 min plasma discharge duration is 74 ± 35 nm. When plasma discharge duration increases to 5 min, the average diameter of nanoseeds increases to 130 ± 65 nm. Further increase of plasma discharge duration leads to larger nanostructure size of 284 ± 145 nm. The broader size distribution is due to the coexistence of growing nanoflowers with fully grown nanoflowers, as shown in Figure 6.

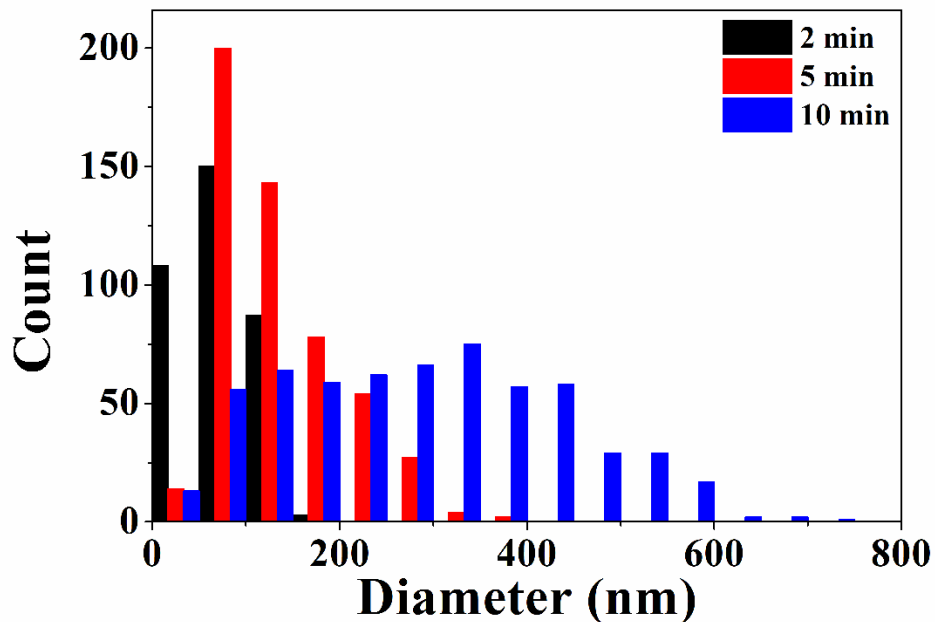


Figure S4 The variation of nanostructure size with increasing plasma discharge duration from 2 min, 5 min to 10 min.

S5. Comparison of surface area between nanoflowers and nanosheets

The contact angles of nanoflowers and nanosheets are shown in Figure S5. Smaller contact angle (43°) for nanoflowers than that of nanosheets (69°) indicates the larger surface area of nanoflowers than that of nanosheets.

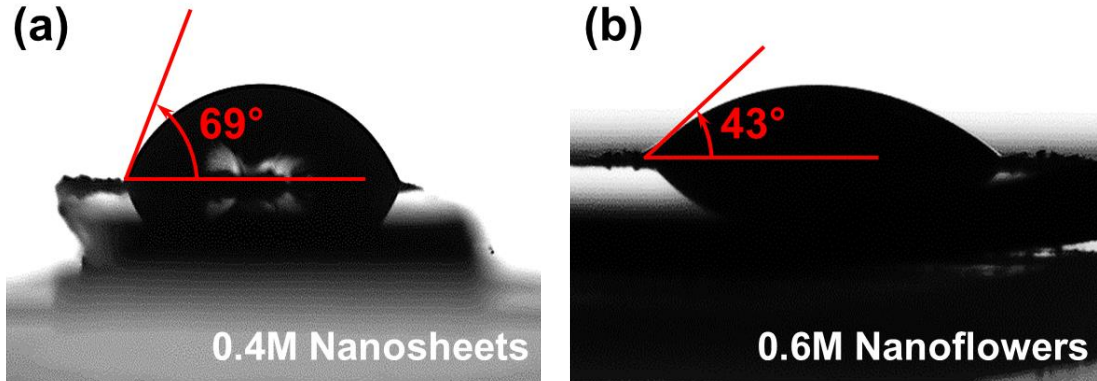


Figure S5 The comparison of contact angles between nanoflowers and nanosheets.

S6. Cyclic voltammograms (CV) of nanoflowers and nanosheets in acidic solution

Figure S6 shows the CV curves of nanoflowers and nanosheets in N₂-saturated 0.5 M H₂SO₄ solution at scan rate of 50 mV·s⁻¹. The current density of nanoflowers is much higher than that of nanosheets, indicating the better activity of 3D nanoflower than 2D nanosheet in acidic environment. The electrochemically active surface area (ECSA) of nanoflowers (5.76 cm²·g_{Pt}⁻¹) is estimated from the CV curve in Figure S6(a) through the following equation according to literature [1]:

$$ECSA(\text{cm}^2_{Pt} \cdot \text{g}_{Pt}^{-1}) = \frac{q_{Pt}(\text{C} \cdot \text{cm}^{-2}_{electrode})}{\Gamma(\mu\text{C} \cdot \text{cm}^{-2}_{Pt}) \cdot L(\text{g}_{Pt} \cdot \text{cm}^{-2}_{electrode})}$$

where the charge density $q_{Pt}(\text{C} \cdot \text{cm}^{-2}_{electrode})$ is obtained from the integrated area of hydrogen adsorption peaks in the CV curves along with the scan rate of 50 mV·s⁻¹, $\Gamma(\mu\text{C} \cdot \text{cm}^{-2}_{Pt})$ is the reference charge density of platinum, normally equaling to 210 $\mu\text{C} \cdot \text{cm}^{-2}_{Pt}$, and $L(\text{g}_{Pt} \cdot \text{cm}^{-2}_{electrode})$ is the Pt content or loading in the electrode. In our work, $L(\text{g}_{Pt} \cdot \text{cm}^{-2}_{electrode})$ is approximately $9.1 \times 10^{-4} \text{ g}_{Pt} \cdot \text{cm}^{-2}_{electrode}$. However, the ECSA of nanosheet sample (0.4 M Co-precursor) could not be estimated through this method since no hydrogen adsorption and desorption are observed in its CV curve (Figure S6(b)).

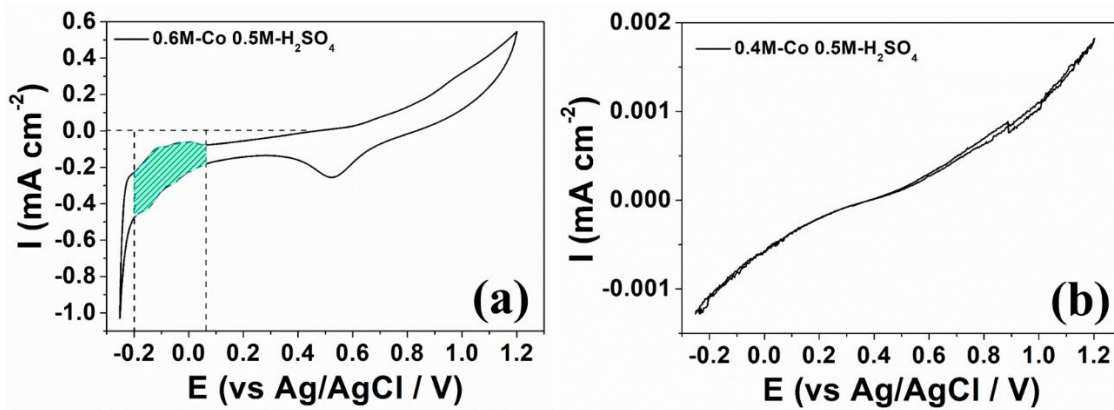


Figure S6 CV curves of (a) nanoflowers (0.6 M CoSO₄) and (b) nanosheets (0.4 M CoSO₄) in N₂-saturated 0.5 M H₂SO₄ solution at scan rate of 50 mV·s⁻¹.

S7. CV curves of Pt₃Co nanoflowers in NaOH solution with different molar concentration and different sweep range

Figure S7(a) shows the CV curves of Pt₃Co nanoflowers in NaOH solution with different molar concentration (0.1 and 0.2 M) and in different sweep range (0.05-1.00 V and 0.05-0.80 V) at a scan rate of 10 mV·s⁻¹. Redox peaks only appears for the CV recorded in 0.2 M NaOH solution, while none redox peaks are shown for 0.1 M NaOH solution (Figure S7(b)). The current density and redox potentials are constant in 0.2 M NaOH solution with sweep range of both 0.05-1.00 V and 0.05-0.80 V. Hence, the rest CV in our work are measured in 0.2 M NaOH with maximum sweep potential of 0.80 V.

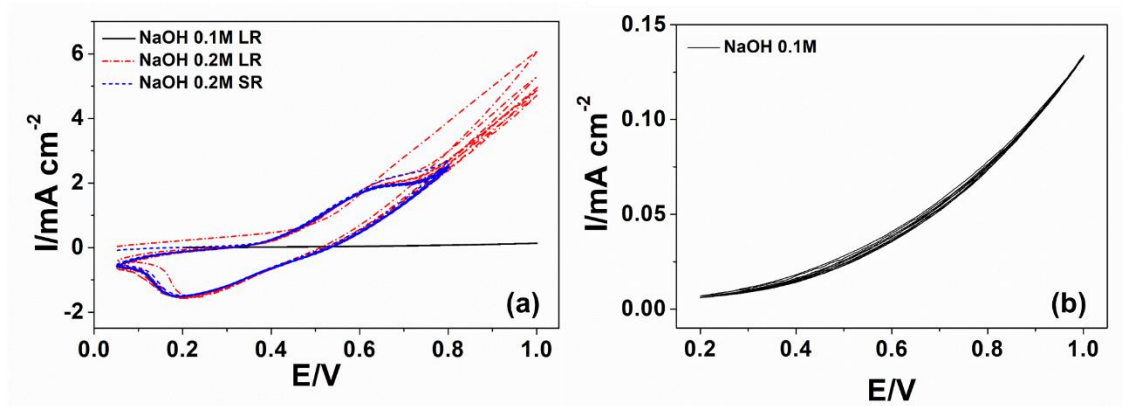


Figure S7 CV curves of Pt₃Co nanoflowers (a) in NaOH solution with different molar concentration (0.1 and 0.2 M) and in different sweep range (0.05-1.00 V and 0.05-0.80 V); (b) in 0.1 M NaOH solution.

References

- [1] Wang W, Wang Z, Yang M, Zhong C-J and Liu C-J 2016 Highly active and stable Pt (111) catalysts synthesized by peptide assisted room temperature electron reduction for oxygen reduction reaction *Nano Energy* **25** 26-33